Nanoscale Research Letters

NANO IDEA Open Access

Hydrothermal Synthesis and Upconversion Properties of About 19 nm Sc_2O_3: Er^{3+}, Yb^{3+} Nanoparticles with Detailed Investigation of the Energy Transfer Mechanism

Fen Li[1], Jing Li[2*], Li Chen[1,2*], Yuxin Huang[2], Yaru Peng[2], Yongshi Luo[3], Ligong Zhang[3] and Jiajia Mu[4]

Abstract

The Sc_2O_3: Er^{3+}, Yb^{3+} nanoparticles (NPs) with the size of about 19 nm were synthesized by a simple oleic acid-mediated hydrothermal (HT) process. X-ray diffraction (XRD), transmission electron microscopy (TEM), upconversion luminescence (UCL) spectra, and decay curves were used to characterize the resulting samples. The Sc_2O_3: Er^{3+}, Yb^{3+} NPs made by HT method exhibit the stronger UCL, of which the red UCL are enhanced by a factor of 4, in comparison with those samples prepared by solvothermal (ST) method at the same optimized lanthanide ion concentrations. The UCL enhancement can be attributed to the reduced surface groups and longer lifetimes. Under 980 nm wavelength excitation, the decay curves of Er^{3+}: ($^2H_{11/2}$, $^4S_{3/2}$) → $^4I_{15/2}$ and $^4F_{9/2}$ → $^4I_{15/2}$ emissions for Sc_2O_3: Er^{3+}, Yb^{3+} NPs samples are both close to each other, resulting from the cross relaxation energy transfer from Er^{3+} to Yb^{3+}, followed by an energy back transfer within the same Er^{3+}-Yb^{3+} pair. Also, under the relatively low-power density, the slopes of the linear plots of log(*I*) vs. log(*P*) for red and green emissions are 2.5 and 2.1, implying the existence of three-photon processes. Our results indicate that Sc_2O_3: Er^{3+}, Yb^{3+} NPs is an excellent material for achieving intense UCL with small size in the biological fields.

Keywords: Sc_2O_3, Hydrothermal synthesis, Upconversion, Energy transfer, Er^{3+}/Yb^{3+}

Introduction

Infrared to visible upconversion luminescence (UCL) has been extensively studied for its fundamental value [1–3] and its various potential applications in upconversion lasers, bioimaging, infrared imaging, solar cells, etc. [4–8]. The co-doping of Er^{3+} and a high concentration of sensitizer Yb^{3+} forms the most attractive energy transfer (ET) upconversion system [1]. Under 980 nm infrared excitation of the sensitizer Yb^{3+}, this system can generate green and red emission originating from the ($^2H_{11/2}$, $^4S_{3/2}$) → $^4I_{15/2}$ and $^4F_{9/2}$ → $^4I_{15/2}$ transitions of Er^{3+}, respectively [9]. Selection of appropriate host material is essential in the synthesis of lanthanide-doped nanocrystals (NCs) with favorable optical properties such as high UC efficiency and controllable emission profile. The practical applications require the development of more efficient, high stability UC materials with low excitation density [10, 11]. Oxide materials are usually very stable chemically, mechanically, and thermally, and could therefore be promising hosts for UC applications [3, 12–16]. The cubic sesquioxide materials (such as Y_2O_3, Lu_2O_3, Sc_2O_3, etc.) display particular structural characteristics and physical properties. For example, Y_2O_3 shows up the outstanding UCL as the typical oxide host [3, 17]. The Sc_2O_3 has the smallest lattice parameter. The short Sc–Sc bond length in Sc_2O_3 can produce the short distance within an Yb^{3+}-Er^{3+} pair, speeding up the Yb^{3+} → Er^{3+} energy transfer. In our previous work, Sc_2O_3: Er^{3+}, Yb^{3+} nanostructures were obtained using a biphasic solvothermal (ST) method [17]. The red UCL in this samples are enhanced, compared with the bulk sample synthesized using a solid-state (SS) reaction. The average crystal size of nanostructures has reduced to about

* Correspondence: lij@ccut.edu.cn; chenli@ccut.edu.cn
[2]School of Materials Science and Engineering, Changchun University of Technology, 2055 Yan'an Street, Changchun 130012, Jilin, China
[1]School of Chemical Engineering & Advanced Institute of Materials Science, Changchun University of Technology, 2055 Yan'an Street, Changchun 130012, Jilin, China
Full list of author information is available at the end of the article

200 nm, which favors the application in fluorescence imaging.

A variety of chemical techniques, including coprecipitation, solvothermal synthesis (ST), hydrothermal method (HT), sol–gel processing, thermal decomposition, etc., have been demonstrated to synthesize lanthanide-doped UC NCs [14, 18–22]. Optimization of synthesis procedure is critical to obtain NCs with tailored crystal size, morphology, surface functionalization, and optical properties. The HT approach is a good choice due to its convenience, exemption from pollution, and the possibility of achieving satisfying crystallinity at a relatively low temperature [23]. Zhao et al. utilized an oleic acid-mediated HT method for the synthesis of UC $NaYF_4$ nanorods, nanotubes, and flower-patterned nanodisks [20]. Chen et al. prepared Fe^{3+} co-doped $NaYF_4$: Er, Yb UC NCs by a HT method using oleic acid as a capping ligand and a surface modifier [24]. In this work, Sc_2O_3: Er^{3+}, Yb^{3+} nanoparticles (NPs) of 19 nm in average diameters have been first synthesized through a simple oleic acid-mediated HT method. We found the stronger UCL in this Sc_2O_3: Er^{3+}, Yb^{3+}NPs samples, of which the red UCL are enhanced by a factor of 4, in comparison with that in the same optimized concentration Sc_2O_3 samples by ST method. The UCL enhancement can be attributed to the reduced surface groups and longer lifetimes. Additionally, the UCL property and mechanism of HT-Sc_2O_3: Er^{3+}, Yb^{3+} NPs were investigated by the spectra distribution, power dependence, and lifetime measurement.

Experimental

Sample Preparation

The Sc_2O_3: Er^{3+}, Yb^{3+} samples were prepared by the HT method via the hydrolysis of relevant mineral salts in an ethanol scheme. The high purity raw materials of Sc_2O_3, Er_2O_3, and Yb_2O_3 powers were dissolved in dilute HNO_3 and deionized water to obtain cationic nitrates solutions, respectively. The $Sc(NO_3)_3$, $Er(NO_3)_3$, and $Yb(NO_3)_3$ solutions with corresponding mole ratios were dissolved in absolute ethanol (20 ml), stirring to form a homogeneous solution. Then an aqueous sodium hydroxide solution (2 ml) was added dropwise to the above mixture with stirring for 30 min, followed by adding oleic acid (1 ml), then vigorous stirring for 1 to 2 h. The resulting suspension was placed in a close Teflon-lined stainless steel autoclave with 50 ml capacity and heated at 180 °C for 24 h. After the autoclave was cooled to room temperature, naturally the precipitate was then centrifuged and washed several times with deionized water and absolute ethanol, respectively. The powder was obtained after being dried in a vacuum oven at 80 °C for 15 h and annealed 700 °C for 2 h. For comparison, we prepared Sc_2O_3 samples prepared by the ST method at the same sintering temperature 700 °C for 2 h [17].

Measurements and Characterization

Powder X-ray diffraction (XRD) datum was collected using Cu-Kα radiation (λ = 1.54056 Å) on an X-ray powder diffractometer (Rigaku D/Max IIA). Transmission electron microscopy (TEM) image was obtained by using a transmission electron microscope (JEM-2000EX) operating at an acceleration voltage of 200 kV. The UCL spectra were recorded with a spectrophotometer (Hitachi F-7000) and infrared spectra were performed by using a Triax 550 spectrometer (Jobin-Yvon) pumped with a power-controllable 980 nm diode laser at room temperature. Infrared spectra in transmission mode were measured on a Thermofisher Nicolet IS50 FT-IR spectrometer, using pressed KBr tablets. In fluorescence lifetime measurements, an optical parametric oscillator (OPO) was tuned to 980 nm as an excitation source, and the signals were detected by a Tektronix digital oscilloscope (TDS 3052).

Results and Discussion

The structures characterized by the XRD patterns are shown in Fig. 1a for samples by HT method with the nominal compositions of Sc_2O_3: 1%Er^{3+}, y%Yb^{3+} (x = 0, 5, 10, 15). The pure phase Sc_2O_3 was synthesized in agreement with JCPDS card 84-1884. The host lattice exhibits the mineral bixbyite structure with the $Ia\bar{3}$ (T^h_2) symmetry [25]. In this structure, Sc^{3+} is sixfold with the effective ionic radius (0.745 Å). The Yb^{3+} ions owned the large ionic radius (0.868 Å) occupy Sc^{3+} sites to expand the lattice cell volume, making XRD peaks shift to smaller angles as Yb^{3+} concentration increases as shown in the magnified patterns of Fig. 1b. To further reveal the morphology and size distribution, the as-prepared Sc_2O_3 samples were characterized by TEM. Figure 2a shows the TEM image of HT-Sc_2O_3: 1%Er^{3+}, 5%Yb^{3+}. We obtained the sphered NPs with relatively uniform size and good monodispersity. Figure 2b depicts the histogram of the size distribution; these data were obtained from the TEM image of more than 300 NPs. The average diameter of NPs was determined to be about 19 nm.

Figure 3 shows the UCL spectra of Sc_2O_3: 1%Er^{3+}, 10%Yb^{3+} (a) and Sc_2O_3: 1%Er^{3+}, 5%Yb^{3+} (b) samples prepared by HT and ST methods under 980 nm excitation with an output power density of 3 mW mm^{-2}. The strong emission bands centered at ~ 550 and 660 nm are attributed to the 4*f* - 4*f* electronic transitions of Er^{3+}: $(^2H_{11/2}, {}^4S_{3/2}) \rightarrow {}^4I_{15/2}$ and $^4F_{9/2} \rightarrow {}^4I_{15/2}$ transitions, respectively. The insets present the digital photographs of corresponding samples. It reveals that UCL has been dramatically enhanced for the HT sample, compared with the ST one. For HT-Sc_2O_3 samples, the calculated enhancement factor of red UCL is around 4, compared with corresponding ST-Sc_2O_3 samples. It is known that the size of samples has an influence on UCL intensity,

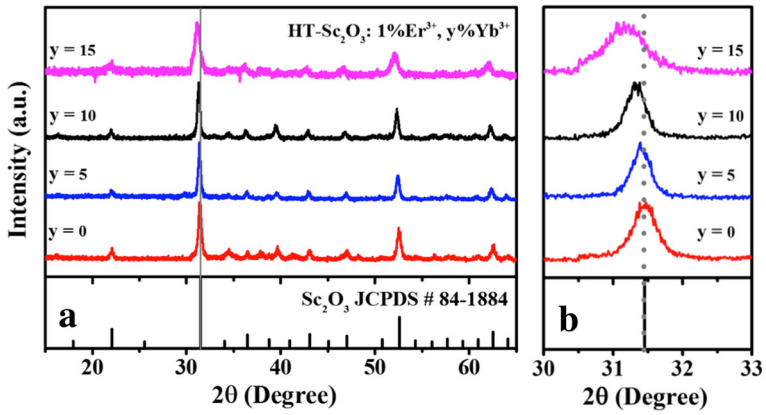

Fig. 1 **a** XRD patterns for HT-Sc_2O_3: 1%Er^{3+}, y%Yb^{3+} ($x = 0$, 5, 10, 15) NPs. **b** Magnified patterns in the diffraction angle ranged from 30° to 33°

which decreased with the decreasing of the size. However, for HT-Sc_2O_3 sample, it owns smaller size and more intensive UCL. It indicates the HT-Sc_2O_3 sample is an excellent material owned intense UCL with small size for the biological fields.

The FTIR spectra of HT-Sc_2O_3: 1%Er^{3+}, 5%/10%Yb^{3+} and ST-Sc_2O_3: 1%Er^{3+}, 5%Yb^{3+}/10%Yb^{3+} samples are shown in Fig. 4. The broad band around 3429 cm^{-1} is attributed to the stretching vibration of –OH in the oleic acid (OA) and water [26, 27]. The 2925 and 2850 cm^{-1} absorption bands are assigned to the asymmetric and symmetric stretching vibrations of the methylene (CH_2) in the long alkyl chain of the OA molecules. The sharpness of the bands indicates that the hydrocarbon chains are well ordered. The anti-symmetric methyl stretch (CH_3) is seen as a shoulder on the peak at 2975 cm^{-1}. The bands at 1200–1750 cm^{-1} can be assigned to the vibrations of C=O in the oleic acid molecule and CO_2 in the air [28]. The transformation to carbonate might have occurred on the surface of crystallites during the heat treatment. These results evidence the existence of capping ligands on the surfaces of samples. Figure 4 shows the absorption intensities of –OH vibration for ST-Sc_2O_3 samples are stronger. The intensities of surface groups for HT/ST-Sc_2O_3: 1%Er^{3+}, 10%Yb^{3+} samples are both stronger than that in co-doped 5%Yb^{3+} samples. The abundant surface groups with available large vibrational quanta may efficiently enhance the MPR processes, inducing the decline of luminescence.

In order to exactly describe the population mechanism in Er^{3+}/Yb^{3+} co-doped HT-Sc_2O_3 sample, the dependence of spectral distributions on the Er^{3+}/Yb^{3+} concentrations has been studied in detail.

The UCL spectra of HT-Sc_2O_3: x%Er^{3+}, 10%Yb^{3+} ($x = 0$, 0.5, 1, 2) under 980 nm excitation are presented in Fig. 5a. For the fixed Yb^{3+} concentration at 10%, the strongest UCL is observed for Er^{3+} concentration around 1%. When Er^{3+} concentration exceeds 1%, the intensity begins to diminish because of the cross relaxation (CR) of Er^{3+} ions [17]. The UCL spectra of HT-Sc_2O_3: 1%Er^{3+}, y%Yb^{3+}, ($y = 0$, 5, 10, 15) are presented in Fig. 5b. For the Er^{3+} singly doped Sc_2O_3, its UC emission is very faint, which has been magnified 100 times. The ET process of $Yb^{3+} \rightarrow Er^{3+}$ plays a dominant role for UCL enhancement. The strongest UCL is observed for Yb^{3+} concentration 5% when fixed the optimal Er^{3+} concentration 1%.

The near infrared emission spectra in the range of 1000–1700 nm for the same variety samples are shown

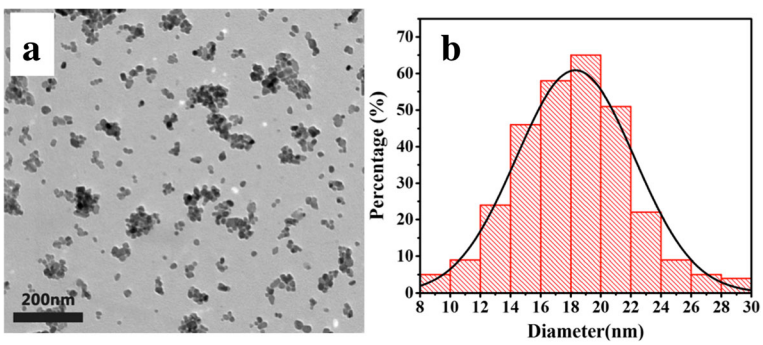

Fig. 2 **a** TEM image and **b** histogram of size distribution of HT-Sc_2O_3: 1%Er^{3+}, 5%Yb^{3+} NPs

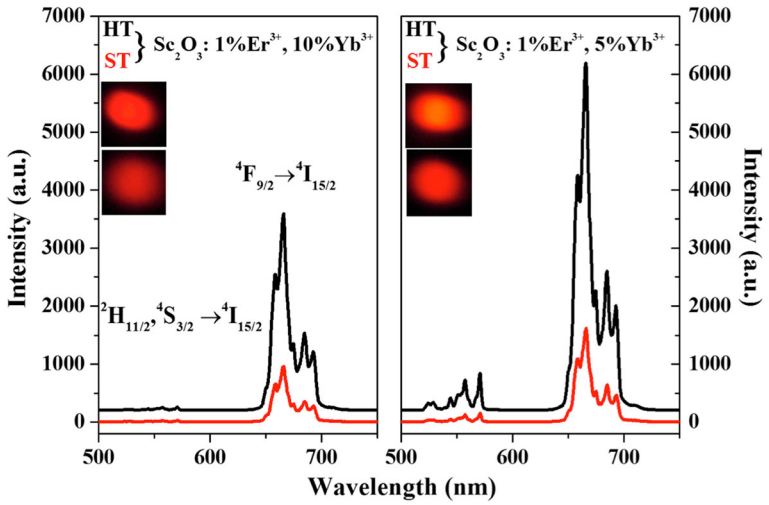

Fig. 3 UCL spectra of Sc_2O_3: 1%Er^{3+}, 10%Yb^{3+} (**a**) and Sc_2O_3: 1%Er^{3+}, 5%Yb^{3+} (**b**) samples prepared by HT and ST methods, respectively, pumped under 980 nm excitation. The insets present the digital photographs of corresponding samples

in Fig. 6. In the Er^{3+}/Yb^{3+} co-doped samples, 980-nm photon excites Yb^{3+}: $^2F_{7/2} \rightarrow {}^2F_{5/2}$ which exhibits fluorescence at 1000–1200 nm exciting Er^{3+} ions into $^4I_{11/2}$ level through a nonresonant phonon-assisted ET process [9]. The Er^{3+} ions in $^4I_{11/2}$ level decay nonradiatively to $^4I_{13/2}$ level, then radiatively to the ground state emitting the photon around 1550 nm [9]. In Fig. 6a, as Er^{3+}-concentration increases, the Yb^{3+} emission has a steady decline which evidences the efficient $Yb^{3+} \rightarrow Er^{3+}$ ET. The Er^{3+} emission gradually increases when Er^{3+} concentration increases from 0 to 1%, then declines slightly as a result of the self-absorption of Er^{3+} ions. In Fig. 6b, Er^{3+}: $^4I_{13/2}$ emission gradually enhances when Yb^{3+} concentration increases from 0 to 5% but subsequently begins to decrease. As Yb^{3+} concentration increases, Yb^{3+} capacity of 980 nm photon absorption is enhanced. The Yb^{3+} emission intensity is shown to increase. Meantime, as the distance of Yb-Yb and Yb-Er pairs decreases, the enhanced energy migration among Yb^{3+} ions speeds up ET from Yb^{3+} to Er^{3+}. It leads to the increased population of Er^{3+}: $^4I_{13/2}$ level but the decreased one of Yb^{3+}: $^2F_{5/2}$level. Due to the quenching of Er^{3+} by Yb^{3+} ions, the emission of Er^{3+}: $^4I_{13/2} \rightarrow {}^4I_{15/2}$ reaches a maximum then drops down.

The pumping power dependences of Er^{3+}: ($^2H_{11/2}$, $^4S_{3/2}$) $\rightarrow {}^4I_{15/2}$ and Er^{3+}: $^4F_{9/2} \rightarrow {}^4I_{15/2}$ intensities in HT-Sc_2O_3: 1%Er^{3+}, 10%Yb^{3+} are measured under 980 nm excitation and plotted in a double logarithmic scales in Fig. 7. For the UCL processes, the UCL intensity (I_{UCL}) depends on the pumping laser power (P) as the equation:

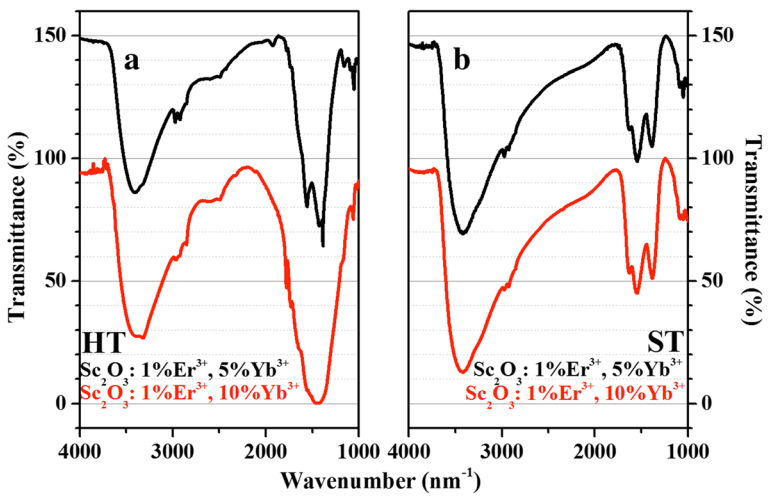

Fig. 4 FTIR spectra of HT-Sc_2O_3: 1%Er^{3+}, 5%/10%Yb^{3+} (**a**) and ST-Sc_2O_3: 1%Er^{3+}, 5%Yb^{3+}/10%Yb^{3+} (**b**) samples

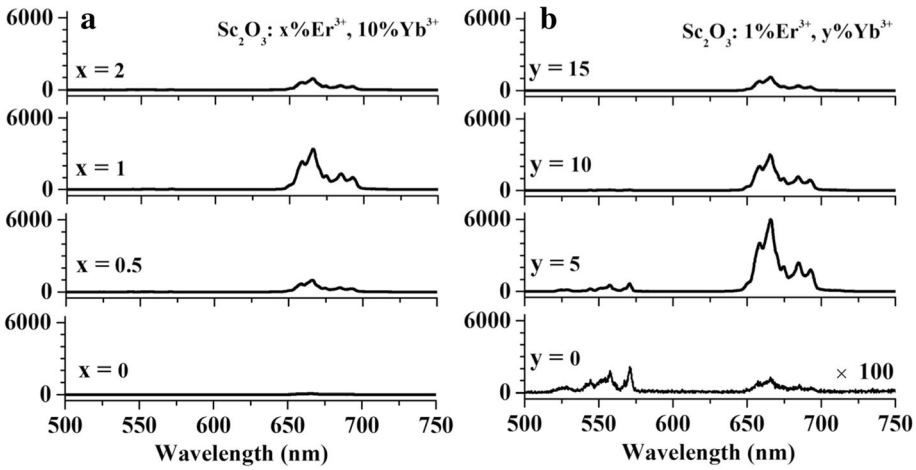

Fig. 5 UCL spectra of HT-Sc_2O_3: x%Er^{3+}, 10%Yb^{3+} ($x = 0$, 0.5, 1, 2) (**a**) and HT-Sc_2O_3: 1%Er^{3+}, y%Yb^{3+}, ($y = 0$, 5, 10, 15) (**b**) under 980 nm excitation

$I_{UCL} \propto Pn$ where n is the number of pumping photons absorbed per upconverted photon emitted [29]. The n value can be obtained from the slope of the linear plots between log (I) and log (P). For the two-step ET process, the n value is theoretically less than 2 due to the competition between linear decay and UC processes. Figure 7 shows the slope n values for red and green emissions are 2.5 and 2.1 in the low pump power density, respectively. It indicates, except for two-step process, that there are also the three-photon processes in HT-Sc_2O_3: 1%Er^{3+}, 10%Yb^{3+} NPs [30, 31].

The upconversion mechanism is drawn in Fig. 8. The ET process is as follows:

The ET①: Yb^{3+}: $^2F_{5/2}$ + Er^{3+}: $^4I_{15/2} \rightarrow Yb^{3+}$: $^2F_{7/2}$ + Er^{3+}: $^4I_{11/2}$

Er^{3+}: $^4I_{11/2} \rightarrow Er^{3+}$: $^4I_{13/2}$ (MPR)

The ET②: Yb^{3+}: $^2F_{5/2}$ + Er^{3+}: $^4I_{13/2} \rightarrow Yb^{3+}$: $^2F_{7/2}$ + Er^{3+}: $^4F_{9/2}$

The ET③: Yb^{3+}: $^2F_{5/2}$ + Er^{3+}: $^4I_{11/2} \rightarrow Yb^{3+}$: $^2F_{7/2}$ + Er^{3+}: $^4F_{7/2}$

Er^{3+}: $^4F_{7/2} \rightarrow Er^{3+}$: ($^2H_{11/2}$, $^4S_{3/2}$) (MPR)

The ET④: Yb^{3+}: $^2F_{5/2}$ + Er^{3+}: $^4F_{9/2} \rightarrow Yb^{3+}$: $^2F_{7/2}$ + Er^{3+}: $^2H_{9/2}$

Er^{3+}: $^2H_{9/2} \rightarrow Er^{3+}$: ($^2H_{11/2}$, $^4S_{3/2}$) (MPR)

Er^{3+}: ($^2H_{11/2}$, $^4S_{3/2}$) $\rightarrow Er^{3+}$: $^4F_{9/2}$ (MPR)

The ET⑤: Yb^{3+}: $^2F_{5/2}$ + Er^{3+}: ($^2H_{11/2}$, $^4S_{3/2}$) $\rightarrow Yb^{3+}$: $^2F_{7/2}$ + Er^{3+}: $^2G_{7/2}$

To verify and make a theoretical interpretation of the UCL results mentioned above, we utilize the simplified steady-state equations.

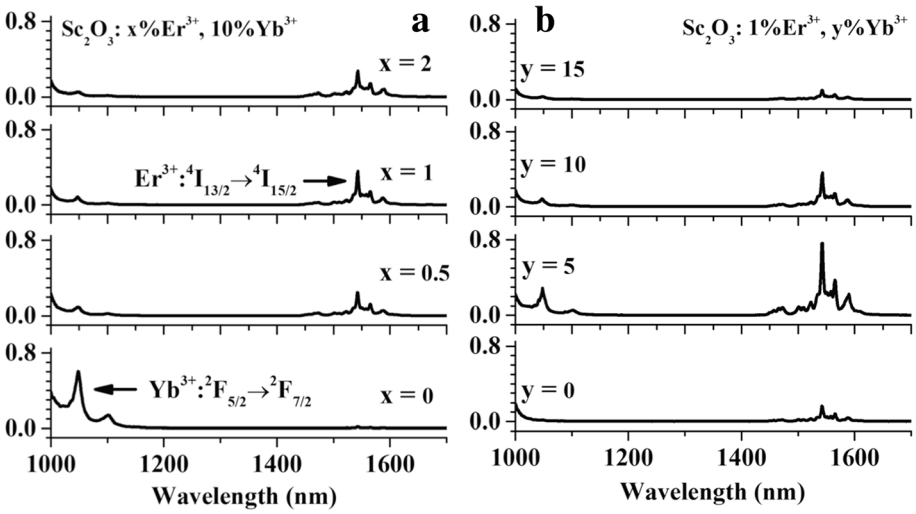

Fig. 6 Near-infrared emission spectra in the range of 1000–1700 nm for HT-Sc_2O_3: x%Er^{3+}, 10%Yb^{3+} ($x = 0$, 0.5, 1, 2) (**a**) and HT-Sc_2O_3: 1%Er^{3+}, y%Yb^{3+}, ($y = 0$, 5, 10, 15) (**b**) under 980 nm excitation

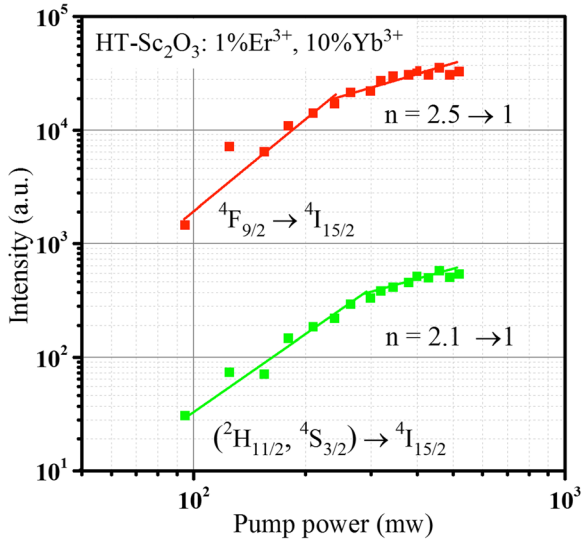

Fig. 7 Power dependence curves for Er^{3+}: ($^2H_{11/2}$, $^4S_{3/2}$) → $^4I_{15/2}$ and $^4F_{9/2} \rightarrow {}^4I_{15/2}$ transitions in HT-Sc_2O_3: 1%Er^{3+}, 10%Yb^{3+} NPs

$$\frac{dn_0}{dt} = 0 \tag{1}$$

$$\frac{dn_1}{dt} = n_2 W_{21} - C_2 N_1 n_1 - \frac{n_1}{\tau_1} \tag{2}$$

$$\frac{dn_2}{dt} = C_1 N_1 n_0 - C_3 N_1 n_2 - n_2 W_{21} - \frac{n_2}{\tau_2} \tag{3}$$

$$\frac{dn_3}{dt} = C_2 N_1 n_1 - C_4 N_1 n_3 - \frac{n_3}{\tau_3} \tag{4}$$

$$\frac{dn_4}{dt} = C_3 N_1 n_2 - C_5 N_1 n_4 - \frac{n_4}{\tau_4} \tag{5}$$

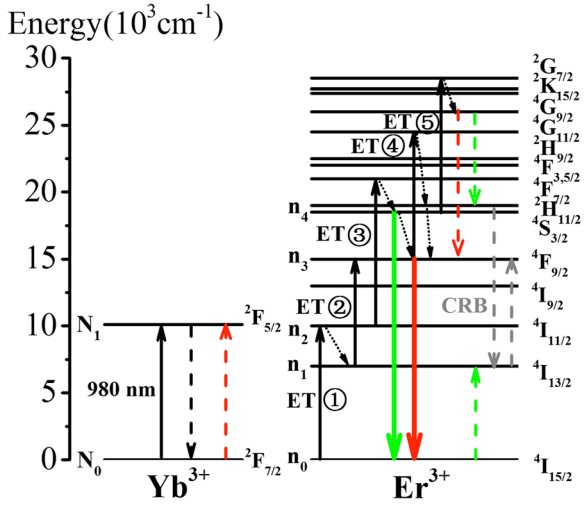

Fig. 8 The energy level diagrams and dominant upconversion mechanism in Sc_2O_3: Er^{3+}, Yb^{3+} NPs under 980 nm pump

$$\frac{dN_1}{dt} = \sigma I N_0 - C_1 N_1 n_0 - C_2 N_1 n_1 - C_3 N_1 n_2 - C_4 N_1 n_3 - C_5 N_1 n_4 - \frac{N_1}{\tau_{Yb}} = 0 \tag{6}$$

Where σ is the absorption cross section of Yb^{3+} ions, I is the incident pumping power, N_i is the population density of the ith level of Yb^{3+}, n_i is the population density of ith level of Er^{3+} involved in the upconversion process, τ_i is the lifetime of ith level of $Er^{3+}$and τ_{Yb} is the lifetime of $^2F_{5/2}$ level of Yb^{3+}, C_i represents the ET coefficient of $Yb^{3+} \rightarrow Er^{3+}$ for steps $i = 1, 2, 3, 4, 5$, and W_{21} represents the non-radiative rate between 1 and 2 levels of the Er^{3+} ions.

Compared with two-step process, the UC efficiency of three-photon processes from NIR to visible is decreased [32]. Additionally, the high-photon process is prominent when pumping power is high enough. The excitations of Er^{3+}: $^4F_{9/2}$ by ET to Er^{3+}: $^2H_{9/2}$ can be neglected due to the weak pump in our experiment. By Eq. (4), the red emission intensity (I_{Red}) can be obtained by

$$I_{Red} = \gamma_3 n_3 = \gamma_3 C_2 \tau_3 I_{Yb} I_{n_1}$$

Due to the CR of the Er^{3+}– Er^{3+} interaction is not considered, the lifetime, τ_3, is a constant. That is to say, $I_{Red} \propto I_{Yb} I_{n_1}$, where I_{Yb} and I_{n1} represent the emission intensity of Yb^{3+}: $^2F_{5/2}$ and Er^{3+}: $^4I_{13/2}$, respectively. The γ_3 is radiative rate of red emission. The calculated I_{Red}values at various Er^{3+}/Yb^{3+}concentrations are presented in Fig. 9, scaled to the maximum. For comparison, the I_{Red} values obtained directly from the UCL emission spectra are also depicted. The calculated and experimental I_{Red} trends are consistent with each other and obtain the best value at the same Er^{3+}/Yb^{3+} concentrations, demonstrating the validity of experimental data.

The three-photon green and red UC processes occurred simultaneously result in the increase of the corresponding n values. Meanwhile, the n value of red UC process increases more effectively than that of green UC process. In Fig. 8, the green and red UCL can be populated by CR, as Er^{3+}: $^4G_{11/2}$ + Er^{3+}: $^4I_{15/2} \rightarrow Er^{3+}$: ($^2H_{11/2}$, $^4S_{3/2}$) + Er^{3+}: $^4I_{13/2}$ and Er^{3+}: $^4G_{11/2}$ + Yb^{3+}: $^2F_{7/2} \rightarrow Er^{3+}$: $^4F_{9/2}$ + Yb^{3+}: $^2F_{5/2}$, respectively [31]. The three-photon green UCL is via a cross-relaxation process between two Er^{3+} ions; however, the cross-relaxation in the three-photon red UCL is between Yb^{3+} and Er^{3+} ions. Since the Yb^{3+} concentration is much higher than Er^{3+} in our experiment, the three-photon red UC process is more effective than the three-photon green UC process, resulting in a rapid increase of n value for red UCL. In addition, it should be noted that all the three-photon processes are few, so the n values deviate obviously from 3. At the high pump power density, two slopes gradually drop to 1 because UC process becomes dominant [33].

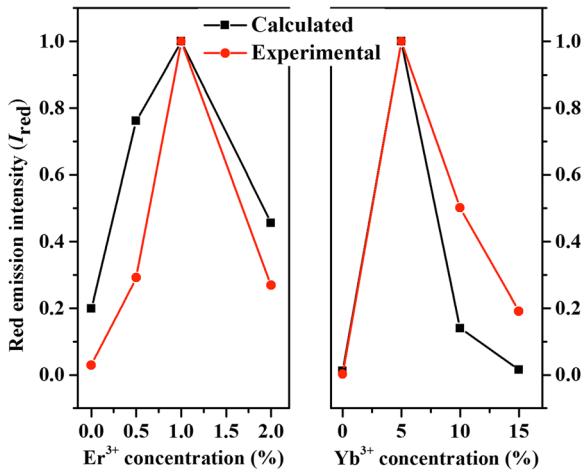

Fig. 9 Calculated and experimental red emission intensities (I_{Red}) values at various Er^{3+}/Yb^{3+}concentrations. The intensities are scaled to the maximum

The decay curves of the Er^{3+}: ($^2H_{11/2}$, $^4S_{3/2}$) → $^4I_{15/2}$ and $^4F_{9/2}$ → $^4I_{15/2}$ transitions in HT-Sc_2O_3 and ST-Sc_2O_3 samples under the 980 nm excitation wavelength have been measured and shown in Fig. 10. The decay times for red and green emissions are calculated by integrating the area under the corresponding decay curves with the normalized initial intensity. Figure 10a, b shows the green and red emission lifetimes in HT-Sc_2O_3: 1%Er^{3+}, 5%Yb^{3+} are longer than those in ST-Sc_2O_3: 1%Er^{3+}, 5%Yb^{3+}. The lifetime is proportional to population of level. The longer values indicate the stronger red and green UCL in HT-Sc_2O_3 sample. In our previous report, we found our samples own the shorter decay lifetime values than that in the literature. Actually, the decay times of Er^{3+}: ($^2H_{11/2}$, $^4S_{3/2}$) → $^4I_{15/2}$ and $^4F_{9/2}$ → $^4I_{15/2}$ emissions for HT/ST-Sc_2O_3: 1%Er^{3+}, 5%Yb^{3+} samples are both close to each other. If Er^{3+}: $^4F_{9/2}$ level is populated by the MPR process from Er^{3+}: ($^2H_{11/2}$, $^4S_{3/2}$) levels, the decay time of Er^{3+}: $^4F_{9/2}$ level approaches to that of Er^{3+}: $^4S_{3/2}$ level. However, this MPR process is inefficient for population of Er^{3+}: $^4F_{9/2}$ level [17]. There is another non-MPR mechanism for populating the Er^{3+}: $^4F_{9/2}$level from Er^{3+}: $^4S_{3/2}$ level. The mechanism involves CR ET: Er^{3+}: ($^2H_{11/2}$, $^4S_{3/2}$) + Yb^{3+}: $^2F_{7/2}$ → Er^{3+}: $^4I_{13/2}$ + Yb^{3+}: $^2F_{5/2}$; then, in the same Er^{3+}–Yb^{3+} pair, an energy back transfer (CRB) Yb^{3+}: $^2F_{5/2}$ + Er^{3+}: $^4I_{13/2}$ → Yb^{3+}: $^2F_{5/2}$ + Er^{3+}: $^4F_{9/2}$occurs [1]. If the CRB process dominates the main way for the population of Er^{3+}: $^4F_{9/2}$ level, the decay time of Er^{3+}: $^4F_{9/2}$ level should be almost equal to the decay time of Er^{3+}: $^4S_{3/2}$ level. The CRB process is fast and efficient at low excitation density.

Figure 11 shows the UCL spectra of three typical sesquioxides under 980 nm excitation. The Sc_2O_3: 1%Er^{3+}, 5%Yb^{3+} sample exhibits the strongest UCL in the series of spectra. Furthermore, the emission line of Er^{3+}: $^4F_{9/2}$ level at the lowest energy side in Sc_2O_3 shifts to the longer wavelength side by 8 nm relative to that in Y_2O_3. The nearest Sc-Sc distance is 3.27 Å in Sc_2O_3 shorter than the Y-Y distance (3.752 Å) in Y_2O_3 [3, 17]. The mean Sc–O bond length (2.121 Å) in Sc_2O_3 is shorter than the mean Y–O bond length (2.263 Å) in Y_2O_3. The Er^{3+}/Yb^{3+} on Sc^{3+} site in Sc_2O_3 experiences a stronger crystal field than on Y^{3+} site in Y_2O_3. The red shift of

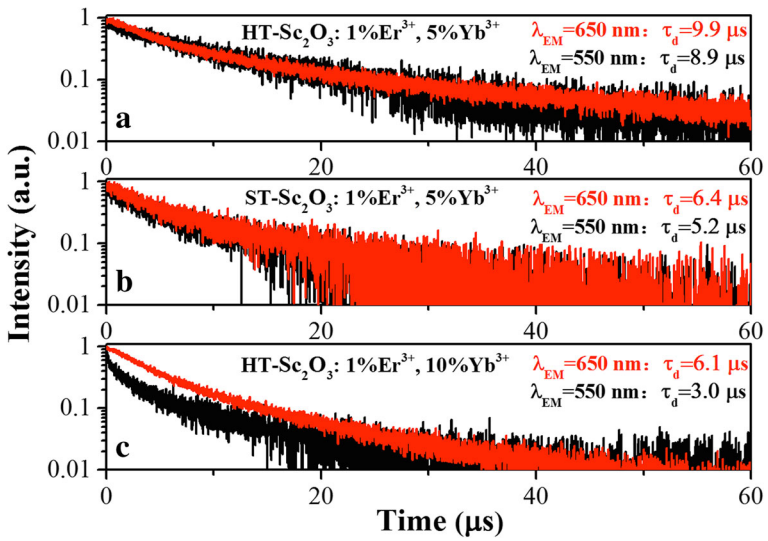

Fig. 10 Decay curves of the Er^{3+}: ($^2H_{11/2}$, $^4S_{3/2}$) → $^4I_{15/2}$ and $^4F_{9/2}$ → $^4I_{15/2}$ transitions in HT-Sc_2O_3 and ST-Sc_2O_3 samples under the 980 nm excitation wavelength

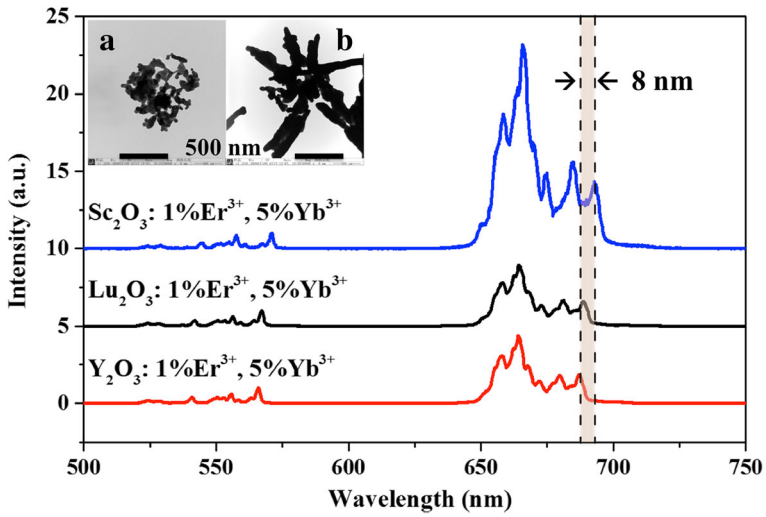

Fig. 11 UCL spectra of Er^{3+}/Yb^{3+} co-doped typical sesquioxide materials under 980 nm excitation

spectrum can be attributed to the large Stark splitting of Er^{3+} ions in Sc_2O_3 host. The morphologies of Y_2O_3 and Lu_2O_3 samples were also characterized by TEM as shown in the inset of Fig. 11a, b, respectively, for comparison. The obtained spherical particles are both agglomerated to bulk. The better dispersion and uniformity of Sc_2O_3 NPs synthesized by HT method favor its application in biological assays and medical image.

Conclusions

In summary, Sc_2O_3: Er^{3+}, Yb^{3+} NPs about 19 nm were synthesized by a simple oleic acid-mediated HT process. The Sc_2O_3: Er^{3+}, Yb^{3+} NPs by HT method shows the stronger UCL, of which the red UCL are enhanced by a factor of 4, in comparison with that in the same optimized concentration Sc_2O_3 samples by ST method. The UCL enhancement can be attributed to the reduced surface groups and longer lifetimes. The surface groups enhanced the MPR, inducing the decline of luminescence. Under the 980 nm excitation, the decay curves of Er^{3+}: ($^2H_{11/2}$, $^4S_{3/2}$) → $^4I_{15/2}$ and $^4F_{9/2}$ → $^4I_{15/2}$ emissions for HT-Sc_2O_3: 1%Er^{3+}, 5%Yb^{3+} samples are close to each other, resulting from the non-MPR mechanism for populating the Er^{3+}: $^4F_{9/2}$ level from Er^{3+}: $^4S_{3/2}$ level. The mechanism involves CR ET: Er^{3+}: ($^2H_{11/2}$, $^4S_{3/2}$) + Yb^{3+}: $^2F_{7/2}$ → Er^{3+}: $^4I_{13/2}$ + Yb^{3+}: $^2F_{5/2}$; then, in the same Er^{3+}–Yb^{3+} pair, an energy back transfer (CRB) Yb^{3+}: $^2F_{5/2}$ + Er^{3+}: $^4I_{13/2}$ → Yb^{3+}: $^2F_{5/2}$ + Er^{3+}: $^4F_{9/2}$ occurs. Under the relatively low-power density, the slopes of the linear plots of log(*I*) vs log(*P*) for red and green emissions are 2.5 and 2.1, respectively, which are larger than 2 because of the existence of three-photon processes. Compared with the typical sesquioxides (Y_2O_3 and Lu_2O_3), the Sc_2O_3: 1%Er^{3+}, 5%Yb^{3+} NPs exhibits the stronger UCL. Furthermore, in Sc_2O_3 the emission line of Er^{3+}: $^4F_{9/2}$ level at the lowest energy side shifts to the longer wavelength side by 8 nm relative to that in Y_2O_3 owing to the large Stark splitting of Er^{3+} ions in Sc_2O_3 host. Results show the Sc_2O_3: Er^{3+}, Yb^{3+} nanoparticles (NPs) is an excellent material for achieving intense UCL with small size in the biological fields.

Abbreviations

CR: Cross relaxation; ET: Energy transfer; HT: Hydrothermal; NCs: Nanocrystals; NPs: Nanoparticles; OPO: Optical parametric oscillator; ST: Solvothermal; TEM: Transmission electron microscopy; UCL: Upconversion luminescence; XRD: X-ray diffraction

Funding

This work is supported by the National Natural Science Foundation of China (Grant No. 11504029 and 11474035), the Jilin Province Science & Technology Department (Grant No. 20170520110JH and 20170520108JH), and 2015 Programming Projects on Scientific Research of Jilin Province Department of Education.

Availability of Data and Materials

The datasets supporting the conclusions of this article are included within the article.

Authors' Contributions

JL and LC contributed to study design. FL and JL performed the experiments, analyzed the data, and wrote the manuscript. YXH, YRP, and JJM participated in the analyses of the results and discussion of this study. LGZ and YSL ensured UCL, FTIR, and OPO assays. All authors read and approved the final manuscript.

Competing Interests

The authors declare that they have no competing interests.

Publisher's Note

Author details

[1]School of Chemical Engineering & Advanced Institute of Materials Science, Changchun University of Technology, 2055 Yan'an Street, Changchun 130012, Jilin, China. [2]School of Materials Science and Engineering,

Changchun University of Technology, 2055 Yan'an Street, Changchun 130012, Jilin, China. [3]State Key Laboratory of Luminescence and Applications, Changchun Institute of Optics, Fine Mechanics and Physics, Chinese Academy of Sciences, 3888 Eastern South Lake Road, Changchun 130033, China. [4]School of Science, Beihua University, 15 Jilin Street, Jilin 132013, Jilin, China.

Received: 25 September 2018 Accepted: 9 November 2018
Published online: 22 November 2018

References

1. Zhang JH, Hao ZD, Li J, Zhang X, Luo YS, Pan GH (2015) Observation of efficient population of the red-emitting state from the green state by non-multiphonon relaxation in the Er^{3+}–Yb^{3+} system. Light Sci Appl 4:e239
2. Qin W-P, Liu Z-Y, Sin C-N, Wu C-F, Qin G-S, Chen Z, Zheng K-Z (2014) Multi-ion cooperative processes in Yb^{3+}clusters. Light Sci Appl 3:e193
3. Li J, Zhang JH, Hao ZD, Zhang X, Zhao JH, Luo YS (2012) Intense upconversion luminescence and origin study in Tm^{3+}/Yb^{3+} codoped calcium scandate. Appl Phys Lett 101:121905
4. Möbert PE-A, Heumann E, Huber G, Chai BHT (1997) Green Er^{3+}: $YLiF_4$ upconversion laser at 551 nm with Yb^{3+} codoping: a novel pumping scheme. Opt Lett 22:1412–1414
5. Zijlmans HJMAA, Bonnet J, Burton J, Kardos K, Vail T, Niedbala RS, Tanke HJ (1999) Detection of cell and tissue surface antigens using up-converting phosphors: a new reporter technology. Anal Biochem 267:30–36
6. Dianoy EM (2012) Bismuth-doped optical fibers: a challenging active medium for near-IR lasers and optical amplifiers. Light Sci Appl 1:e12
7. Liang Y-J, Liu F, Chen Y-F, Wang X-J, Sun K-N, Pan ZW (2016) New function of the Yb^{3+}ion as an efficient emitter of persistent luminescence in the short-wave infrared. Light Sci Appl 5:e16124
8. Lv RC, Yang PP, Hu B, Xu JT, Shang WT, Tian J (2017) In situ growth strategy to integrate up-conversion nanoparticles with ultrasmall CuS for photothermal theranostics. ACS Nano 11:1064–1072
9. Auzel F (2004) Upconversion and anti-stokes processes with f and d ions in solids. Chem Rev 104(1):139–174
10. Wang F, Liu XG (2009) Recent advances in the chemistry of lanthanide-doped upconversion nanocrystals. Chem Soc Rev 38:976–989
11. Teng X, Zhu YH, Wei W, Wang SC, Huang JF, Naccache R, Hu WB, Tok AIY, Han Y, Zhang QC, Fan QL, Huang W, Capobianco JA, Huang L (2012) Lanthanide-doped Na_xScF_{3+x} nanocrystals: crystal structure evolution and multicolor tuning. J Am Chem Soc 134:8340–8343
12. Etchart I, Huignard A, Bérard M, Nordin MN, Hernández I, Curry RJ, Gillin WP, Cheetham AK (2010) Oxide phosphors for efficient light upconversion: $Yb^{3+}$and Er^{3+} co-doped Ln_2BaZnO_5(Ln =Y, Gd). J Mater Chem 20:3989–3994
13. Dong B, Cao BS, He YY, Liu Z, Li ZP, Feng ZQ (2012) Temperature sensing and in vivo imaging by molybdenum sensitized visible Upconversion luminescence of rare-earth oxides. Adv Mater 24:1987
14. Paik T, Gordon TR, Prantner AM, Yun H, Murray CB (2013) Designing tripodal and triangular gadolinium oxide Nanoplates and self-assembled Nanofibrils as potential multimodal bioimaging probes. ACS Nano 7(3):2850–2859
15. Li T, Guo CF, Lin L (2013) Up-conversion luminescence of Er^{3+}-Yb^{3+} co-doped $CaIn_2O_4$. Opt Exp 21:18281
16. Ruan JF, Yang ZW, Huang AJ, Zhang HL, Qiu JB, Song ZG (2018) Thermal-chromic reaction induced reversible upconversion emission modulation for switching devices and tunable upconversion emission based on defect engineering of WO_3: Yb3+, Er3+ phosphor. ACS Appl Mater Interfaces 10:14941–14947
17. Jiu JX, An XT, Li J, Leng J, Lü W, Chen L, Wang XJ (2017) Intense red upconversion luminescence and dynamical processes in Sc_2O_3: Yb^{3+}, Er^{3+} nanostructure. Dalton Trans 46:15954–15960
18. Ma YJ, Yang ZW, Zhang HL, Qiu JB, Song ZH (2018) Preparation, growth mechanism, upconversion, and near-infrared photoluminescence properties of convex-lens-like $NaYF_4$ microcrystals doped with various rare earth ions excited at 808 nm. Cryst Growth Des 18:1758–1767
19. Boyer J-C, Vetrone F, Cuccia LA, Capobianco JA (2006) Synthesis of colloidal upconverting NaYF4 nanocrystals doped with Er^{3+}, Yb^{3+} and Tm^{3+}, Yb^{3+} via thermal decomposition of lanthanide trifluoroacetate precursors. J Am Chem Soc 128(23):7444–7445
20. Zhang F, Wan Y, Yu T, Zhang FQ, Shi YF, Xie SH, Li YG, Xu L, Tu B, Zhao DY (2007) Uniform nanostructured arrays of sodium rare-earth fluorides for highly efficient multicolor Upconversion luminescence. Angew Chem Int Ed 46:7976
21. Venkatramu V, Falcomer D, Speghini A, Bettinelli M, Jayasankar CK (2008) Synthesis and luminescence properties of Er^{3+}-doped $Lu_3Ga_5O_{12}$ nanocrystals. J Lumin 128:811–813
22. Xiang GT, Zhang JH, Hao ZD, Zhang X, Pan G-H, Chen L, Luo YS, Lü SZ, Zhao HF (2015) Solvothermal synthesis and upconversion properties of about 10 nm orthorhombic LuF_3: Yb^{3+}, Er^{3+} rectangular nanocrystals. J. Colloid Interface Sci 459:224–229
23. Li YQ, Zhang JH, Zhang X, Luo YS, Ren XG, Zhao HF, Wang XJ, Sun LD, Yan CH (2009) Near-infrared to visible upconversion in Er^{3+} and Yb^{3+} codoped Lu_2O_3 nanocrystals: enhanced red color upconversion and three-photon process in green color upconversion. J Phys Chem C 113:4413–4418
24. Tang J, Chen L, Li J, Wang Z, Zhang JH, Zhang LG, Luo YS, Wang XJ (2015) Selectively enhanced red upconversion luminescence and phase/size manipulation via Fe^{3+} doping in $NaYF_4$: Yb, Er nanocrystals. Nanoscale 7: 14752–14759
25. Lupei V, Lupei A, Gheorghe C, Ikesue A, Osiac E (2009) Energy transfer-driven infrared emission processes in rare earth-doped Sc_2O_3 ceramics. J Lumin 129:1862–1865
26. Liu JF, Li YD (2007) Synthesis and self-assembly of luminescent Ln^{3+}-doped $LaVO_4$ uniform nanocrystals. Adv Mater 19:1118–1122
27. Chen DQ, Yu YL, Huang F, Yang AP, Wang YS (2011) Lanthanide activator doped $NaYb_{1-x}Gd_xF_4$ nanocrystals with tunable down-, up-conversion luminescence and paramagnetic properties. J Mater Chem 21:6186–6192
28. Söderlind F, Pedersen H, Petoral RM Jr, Käll P-O, Uvdal K (2005) Synthesis and characterisation of Gd_2O_3 nanocrystals functionalized by organic acids. J Colloid Interface Sci 288:140–148
29. Pollnau M, Gamelin DR, Lüthi SR, Güdel HU, Hehlen MP (2000) Power dependence of upconversion luminescence in lanthanide and transition-metal-ion systems. Phys Rev B 61:3337
30. Song F, Zhang GY, Shang MR, Tan H, Yang J, Meng FZ (2001) Three-photon phenomena in the upconversion luminescence of erbium–ytterbium-codoped phosphate glass. Appl Phys Lett 79(12):1748–1750
31. Xiang GT, Zhang JH, Hao ZD, Zhang X, Pan G-H, Luo YS, Zhao HF (2015) Decrease in particle size and enhancement of upconversion emission through Y^{3+} ions doping in hexagonal $NaLuF_4$:Yb^{3+}/Er^{3+}nanocrystals. Cryst Eng Comm 17:3103–3109
32. Suyver JF, Aebischer A, Biner D, Gerner P, Grimm J, Heer S, Krämer KW, Reinhard C, Güdel HU (2005) Novel materials doped with trivalent lanthanides and transition metal ions showing near-infrared to visible photon upconversion. Opt Mater 27:1111–1130
33. Suyver JF, Aebischer A, García-Revilla S, Gerner P, Güdel HU (2005) Anomalous power dependence of sensitized upconversion luminescence. Phys Rev B 71:125123